



# Modeling of Micro- and Nanoparticle Characteristics in DC Suspension Plasma Spray

Xue-ming Shao, Kai Zhang, and Hong-bing Xiong

(Submitted October 30, 2013; in revised form October 17, 2014)

Suspension plasma spray is a promising technology for surface coatings. In this work, a comprehensive numerical model was developed to investigate the multiphase flow of suspension droplets and nanoparticles in direct-current (DC) plasma spraying. A three-dimensional computational model was developed to describe the plasma jet flow fields coupled with the axial injection of suspension droplets in which the zirconia micro- and nanoparticles were dispersed. The suspension droplets were tracked using Lagrangian coordinates, considering particle heating, melting, and evaporation. After evaporation of the solvent surrounding the particle, the nanoparticles were discharged into the plasma flow. In addition to the viscous force exerted by the flow on the micrometer-sized particles, the Brownian force and the Saffman lift force were taken into account. The effects of the noncontinuum on particle momentum transfer and evaporation on heat transfer were also considered. The numerical predictions of gas flow temperature were compared with experimental data and numerical data obtained with a different computational fluid dynamics code. The agreement was reasonable. The trajectories, velocity, and temperature of nanoparticles were calculated, and compared with those of microparticles. The results showed that the Brownian force plays a major role in acceleration and heating of nanoparticles. Compared with the conventional plasma spray process with micrometer-sized feedstock, the nanoparticles in suspension plasma spraying were found to have a wider spatial distribution and higher temperature. The effects of operating parameters, such as the power input to the plasma gas and plasma gas composition, on the gas velocity and temperature were investigated. The parameters that have a significant effect on the heat and momentum transfer to the particles injected in the plasma jet were identified.

**Keywords** Lagrangian method, particle force, plasma spray, suspension plasma spraying, two-phase flow

## 1. Introduction

Suspension plasma spray (SPS) is a newly developed technology for surface processing that has attracted increasing attention in recent decades (Ref 1-4). It uses much finer particles, to achieve finely structured coatings. As a result, coatings with improved characteristics, such as high adhesion and low porosity, can be obtained (Ref 5). Compared with coatings made by conventional thermal spraying, nanostructured coatings have superior resistance to wear, erosion, and cracking (Ref 6).

The SPS process involves liquid feedstock preparation and injection into a plasma jet, liquid atomization, plasma jet generation, and interaction of the plasma jet with the droplets and particles. In this process, submicrometer particles are usually dispersed in a solvent, and injected into the plasma jet by an atomization device. After the

X. Shao, Kai Zhang, and H. Xiong, Department of Mechanics, Zhejiang University, Hangzhou 310027, China. Contact e-mail: hbxiang@zju.edu.cn.

Nomenclature	
$C_p$	Specific heat (J/kg/K)
$C_D$	Drag coefficient
$D$	Diffusion coefficients ( $m^2 s^{-1}$ )
$h$	Heat transfer coefficient ( $W/m^2/K$ )
$k$	Thermal conductivity ( $W/m/K$ )
$L_m$	Latent heat of fusion (J/kg)
$L_v$	Latent heat of evaporation (J/kg)
$Nu$	Nusselt number, $Nu = 2 h/k$
$Pr$	Prandtl number, $Pr = \mu C_p/k$
$Q_{conv}$	Convective heat rate (W)
$Q_{rad}$	Radiative heat rate (W)
$Q_{vap}$	Vaporization heat rate (W)
$Sc$	Schmidt number, $Sc = \mu/\rho D$
$r$	Radial coordinate (m)
$R$	Particle radius (m)
$t$	Time (s)
$T_p$	Particle temperature (K)
$T_{m,d}$	Droplet evaporation temperature (K)
$V$	Velocity (m/s)
$Y$	Mass fraction of vapor in the gas phase
Greek Symbols	
$\alpha$	Weight fraction
$\mu$	Viscosity (kg/s/m)

Subscripts	
d	Suspension droplet embedded with nanoparticles
f	Film temperature around the particle
g	Plasma gas
p	Solid nanoparticles or agglomerates
sl	Solvent
$\infty$	Ambient condition of spray

droplets are evaporated in the plasma environment, the submicrometer particles will be discharged into the plasma jet. Such droplets and particles generally have a broad size range (Ref 7) and, thus, may have different trajectories and heat treatment.

Research studies have previously been conducted to understand the mechanisms that govern the particles' behavior in SPS both experimentally (Ref 8-11) and numerically (Ref 12-17). Ozturk et al. (Ref 12) studied the physical process of vaporization of a single drop with convection in high-temperature jets. Marchand et al. (Ref 13) developed a three-dimensional (3D) numerical model to examine the effect of the arc voltage fluctuation on the droplet characteristics. Ahmed et al. (Ref 14) studied the oxidation mechanisms based on the in-flight mass transport and chemical reaction in composite particles. Basu et al. (Ref 15) investigated the effects of droplet size, solute concentration, and plasma temperature on the heat and mass transfer within individual droplets. More recently, Shan et al. (Ref 16) developed a mathematical model to analyze the heat and mass transfer within an evaporating solution droplet in a direct-current (DC) plasma jet. Jabbari et al. (Ref 17) studied suspension injection in the plasma spray process using the Kelvin-Helmholtz Rayleigh-Taylor breakup model. However, these former modeling studies cover only a small range of particle size. As regards suspension feeding, micro- and nanoparticles coexist in the spray system, making it more complex. Systematic analysis of micro- and nanoparticle behavior in a suspension spray has not been attempted yet. Thus, it is necessary to develop a comprehensive numerical model to describe the energy transport process and predict the micro- and nanoparticle characteristics from the operating conditions of the plasma spray system.

This paper presents a numerical model of the in-flight behavior of micro- and nanoparticles in SPS. Firstly, the plasma gas field is calculated based on the Eulerian method to provide environmental information for the particles. Then, the injected droplets with suspended particles are tracked in a Lagrangian scheme, including particle acceleration, suspension droplet heating, nanoparticle heating, melting, and evaporation. The comprehensive particle model is used to predict the nanoparticle trajectory, velocity, and temperature in different in-flight stages for different particle sizes. The effects of the initial particle size on the particle acceleration and heating process are investigated. Finally, the main operating parameters that influence the particle characteristics are indicated.

## 2. Mathematical Model

The thermofluidic fields of the plasma jet were calculated using a Eulerian method, and the particles were treated as Lagrangian entities.

The plasma jet provides the source of acceleration and heating for droplets and particles; it is simulated by using the LAVA code developed by Idaho National Engineering Laboratory (Ref 18). The Navier-Stokes (N-S) equations of the plasma jet were solved, using the assumption that the plasma jet is a continuum, multi-component, compressible, ideal gas, in local thermodynamic equilibrium (LTE), and with temperature-dependent transport properties. Turbulence was simulated using the  $k-\epsilon$  model.

The trajectory, heating, melting, and evaporation of the particles injected into the plasma jet were tracked during the flight in the plasma jet. This study considered the different forces applied to the particles including drag, Saffman lift, and Brownian force. The Knudsen effect and mass evaporation effect on the drag coefficient and Nusselt number were also taken into account.

### 2.1 Particle Acceleration and Tracking

The forces applied on the particles in the plasma jet include the drag force, Saffman lift force, Brownian force, pressure gradient force, and thermophoretic force. The pressure gradient force is negligible in the small-scale jet flow. The thermophoretic force might be important for particles in a high-temperature plasma jet but was neglected in this study for simplicity. For particles smaller than 100  $\mu\text{m}$ , the drag force is prominent. However, near the substrate, the Saffman lift force can be important as well as the Brownian force for the submicro- and nanoparticles. These three forces can be expressed as

$$\begin{aligned} \vec{F}_p = m_p \frac{d\vec{V}_p}{dt} = & \pi r_p^2 C_D f_{\text{Kn}}^{0.45} f_{\text{prop}}^{-0.45} \frac{\rho \left| \vec{V}_g - \vec{V}_p \right| (\vec{V}_g - \vec{V}_p)}{2} \\ & + \frac{2K_c (\eta/\rho_g)^{0.5} d_{ij} \rho_g}{\rho_p d_p (d_{ik} d_{kl})^{0.25}} (\vec{V}_g - \vec{V}_p) + G_0 \sqrt{\frac{\pi S_0}{\Delta t}}, \end{aligned} \quad (\text{Eq 1})$$

where  $f_{\text{prop}}$  is the factor representing the effects of variable plasma properties in the boundary layer surrounding the particle, expressed as  $f_{\text{prop}} = \frac{\rho_c \mu_c}{\rho_w \mu_w}$  (Ref 19), and  $V_g$  is the gas velocity including the turbulent fluctuation calculated from the gas turbulence model. During particle tracking, the turbulent dispersion of particles is calculated by integrating the trajectory equations for individual particles, using the instantaneous fluid velocity along the particle path.  $C_D$  is the drag force coefficient, expressed by (Ref 20)

$$C_D = \left( \frac{24}{\text{Re}_p} + \frac{6}{1 + \sqrt{\text{Re}_p}} + 0.4 \right), \quad (\text{Eq 2})$$

where the particle Reynolds number  $Re_p$  is defined by

$$Re_p = 2\rho_f r_p \left| \vec{V} - \vec{V}_p \right| / \mu_f; \quad (\text{Eq 3})$$

$f_{Kn}$  in Eq (1) represents the noncontinuum effect, which can be expressed by

$$f_{Kn} = \left[ 1 + \left( \frac{2-a}{a} \right) \left( \frac{\gamma_w}{1+\gamma_w} \right) \frac{4}{Pr_w} Kn \right]^{-1}, \quad (\text{Eq 4})$$

where  $a$  is the thermal accommodation coefficient, usually equal to 0.8 (Ref 21),  $Pr_w$  is the Prandtl number, and  $Kn$  is the Knudsen number. For nanoparticles,  $f_{Kn}$  ranges from 0.005 to 0.1 (Ref 22), while for the agglomerates and microsized particles,  $f_{Kn}$  ranges from 0.994 to 0.996 (Ref 23).

The second and third terms on the right-hand side of Eq (1) are the Saffman lift force and the Brownian force, respectively, where  $K_c = 2.594$  is the constant in the Saffman lift force (Ref 24-26),  $d_{ij}$  is the deformation tensor, and  $G_0$  is a zero-mean, unit-variance independent Gaussian random number.  $S_0$  is the spectral intensity  $S_0 = \frac{216\eta\sigma_B T_E}{32\pi^2 r_p^2 \rho_p^2 C_c}$ , and  $\sigma_B$  is the Boltzmann constant,  $\sigma_B = 1.38 \times 10^{-23}$  J/K.

Equation (1) was used to calculate the particle velocity and trajectory and thus infer the evolution of local gas conditions around the particle that will be used to calculate the particle heating.

## 2.2 Heating of Suspension Droplets

The nanoparticles were supposed to be randomly suspended in the droplets, as shown in Fig. 1. The heating model of the droplets neglected thermal conduction in the droplets and used the lumped thermal capacity model, the Biot number in this study being less than  $3 \times 10^{-3}$ . The droplet temperature evolution can be expressed by

$$T_d = T_{d,0} + \frac{Q_d}{m_d C_{p,d}} t \quad \text{if } Q_d < m_d C_{p,d} (T_{m,d} - T_{d,0}),$$

$$T_d = T_{m,d} \quad \text{if } Q_d \leq m_d C_{p,d} (T_{m,d} - T_{d,0}) + m_d \alpha_{sl} L_{v,sl},$$

(Eq 5)

where  $T_{d,0}$ ,  $Q_d$ ,  $m_d$ , and  $C_{p,d}$  are the initial droplet temperature, heat gain, mass, and specific heat of the droplet, respectively.  $Q_d$  can be calculated as  $Q_d = Q_{conv} - Q_{rad}$ , where  $Q_{conv}$  represents the convective heat from the plasma jet, and  $Q_{rad}$  the radiative heat lost by the particle. The calculation of the specific heat  $C_{p,d}$  is based on the

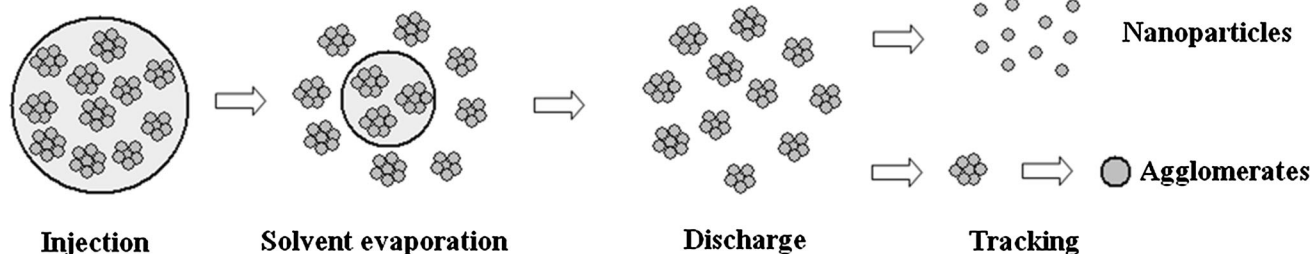


Fig. 1 Schematic of nanoparticle injection, discharge, and tracking

average of the mass fraction of a solid particle and solvent as  $C_{p,d} = C_{p,p}(1 - \alpha_{sl}) + C_{p,sl}\alpha_{sl}$ .

As shown in Fig. 1, once the solvent is totally vaporized, the solid nanoparticles contained in the droplet are discharged in the plasma jet. They then form small pieces of aggregates or individual nanoparticles due to the further evaporation of the solvent and aerodynamic forces of the plasma gas acting on the aggregates. Such phenomena have been observed in experiments (Ref 3). These nanoparticles and agglomerates are treated as new Lagrangian entities with the current parameters of position, velocity, and temperature. In this study, the potential agglomeration of nanoparticles into agglomerates was not considered. The difference between nanoparticles and agglomerates lies in the particle size, and a broad particle size range, i.e., from 1 nm to 1000 nm, was taken into account.

## 2.3 Heating, Melting, and Evaporation of Nanoparticles

A one-dimensional model was used for heating and melting of nanoparticles, assuming a spherical shape, as in Fig. 2. The internal convection within the molten part of the particle was neglected. The temperature distribution inside the particle was described as follows:

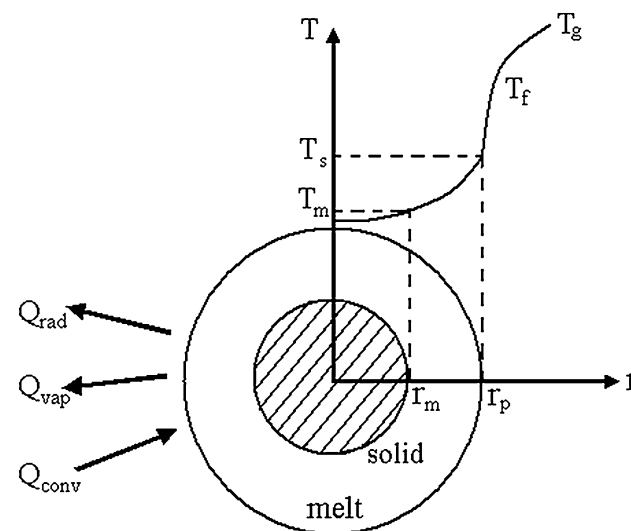


Fig. 2 Schematic of particle heat transfer

$$\rho_p C_p \frac{\partial T_p}{\partial r} = \frac{1}{r^2} \frac{\partial}{\partial r} \left( k_p r^2 \frac{\partial T_p}{\partial r} \right). \quad (\text{Eq 6})$$

The boundary conditions were zero temperature gradient at the particle center, and heat flux at the particle surface expressed as (Ref 27)

$$\frac{\partial T_p}{\partial r} \Big|_{r=0} = 0 \text{ and } 4\pi r_p^2 \left( k_p \frac{\partial T_p}{\partial r} \right) \Big|_{r=r_p} = \dot{Q}_{\text{conv}} - \dot{Q}_{\text{vap}} - \dot{Q}_{\text{rad}}, \quad (\text{Eq 7})$$

where the convective, radiative, and evaporative heat rates  $\dot{Q}_{\text{conv}}$ ,  $\dot{Q}_{\text{vap}}$ , and  $\dot{Q}_{\text{rad}}$  are expressed as  $4\pi r_p^2 h_f (T_f - T_s)$ ,  $\dot{m}_v L_v$ , and  $4\pi r_p^2 \epsilon_p \sigma_s (T_s^4 - T_\infty^4)$ , respectively. The film temperature,  $T_f$ , was defined as  $(T_s + T_g)/2$ , as shown in Fig. 2, being introduced to deal with the steep temperature gradient in the boundary layer around the particle. Radiation between the particle surface and the environment was considered using an optically thin plasma gas. At the film temperature, the heat transfer coefficient,  $h_f$ , was calculated from (Ref 28)

$$\text{Nu} = \frac{2h_f r_p}{k_f} = \left( 2.0 + 0.6 \text{Re}^{1/2} \text{Pr}^{1/3} \right) f_{\text{prop}} f_{\text{Kn}} f_v, \quad (\text{Eq 8})$$

where  $f_v$  accounts for the effect of mass transfer due to evaporation as

$$f_v = \frac{\dot{m}_v c_{p,f} / 2\pi r_p k_f}{\exp\{\dot{m}_v c_{p,f} / 2\pi r_p k_f\} - 1}; \quad (\text{Eq 9})$$

$f_v$  approaches 1 when the evaporation mass rate  $\dot{m}_v$  is close to zero.  $f_v$  is smaller than 1 when  $\dot{m}_v$  is larger than zero. This indicates that the convective heat flux becomes smaller when accounting for evaporation. An additional constraint of energy balance at the melting interface  $r_m$  was also considered as follows:

$$\left( k_p \frac{\partial T_p}{\partial r} \right) \Big|_{r=r_m^-} - \left( k_p \frac{\partial T_p}{\partial r} \right) \Big|_{r=r_m^+} = L_m \rho_p \frac{dr_m}{dt}. \quad (\text{Eq 10})$$

The evaporation mass rate,  $\dot{m}_v$ , is controlled by either vapor diffusion or heat transfer through the boundary layer around the particle. When the particles are heated to melting point in the plasma gas, the vapor diffusion rate through the boundary layer is low and the heat gain of the particle is large enough to meet the latent heat of vaporization. However, when the particle surface temperature approaches boiling point, the vapor diffusion rate could be so high that the energy needed to overcome the latent heat of vaporization is balanced by the net heat transfer to the particle. Therefore, the evaporation rate is limited by the minimum vapor diffusion rate and the net heat gain of the particle is as follows:

$$\dot{m}_v = \min \left\{ 2(\bar{\rho} D_g)_f \pi r_p \ln(1+B) \text{Sh}, \quad \dot{Q}_{\text{net}} / L_v \right\}, \quad (\text{Eq 11})$$

where  $D_g$  is the mass transfer coefficient,  $D_g = \frac{h_g}{\bar{\rho}_g \text{Sc}}$  (Ref 27), Sh is the Sherwood number representing convective mass transfer,  $\text{Sh} = 2.0 + 0.6 \text{Re}_p^{1/2} \text{Sc}$ , and  $B$  is the

mass transfer number,  $B = \frac{Y_p - Y_\infty}{1 - Y_p}$ , which is related to the mass fraction of vapor in the gas phase  $Y_p$  at the particle surface and  $Y_\infty$  at the distance.

### 3. Numerical Setup

This study was conducted with a direct-current SPS system with axial injection of liquid feedstock as illustrated in Fig. 3. The operating parameters of this gun are listed in Table 1.  $\text{ZrO}_2$  particles with different sizes ranging from 1 to 1000 nm (1  $\mu\text{m}$ ) were suspended in alcohol solvent and axially sprayed into the plasma jet. The particle properties are listed in Table 2, and the solvent properties in Table 3.

At the nozzle exit, the velocity and temperature of the plasma gas were expressed by the following formulae (Ref 18):

$$v(r) = V_{\text{cl}} \left[ 1 - (r/R_i)^{1.2} \right],$$

$$T(r) = (T_{\text{cl}} - T_w) \left[ 1 - (r/R_i)^6 \right] + T_w,$$

where  $R_i$  is radius of the inlet nozzle.  $V_{\text{cl}}$  and  $T_{\text{cl}}$  are the velocity and temperature on the nozzle axis; they are calculated from the mass flow rate and thermal energy

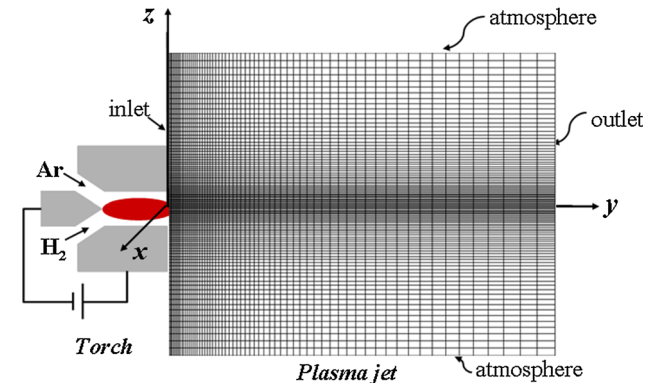


Fig. 3 Computational domain of plasma jet

Table 1 Baseline operating conditions of single-particle injection

Parameter	Value
Plasma gas conditions	
Total plasma gas flow rate (slm)	240
Gas composition: Ar, H <sub>2</sub>	85, 15%
Electrical power input (kW)	50, 80
Feedstock conditions (ZrO <sub>2</sub> )	
Solid content in suspension	10%
Initial nanoparticle size (nm)	1, 10, 100, 1000
Initial suspension droplet radius ( $\mu\text{m}$ )	25
Standoff distance (cm)	5

Note "slm" means standard liters per minute: 1 slm = 16.67 cm<sup>3</sup>/s



**Table 2 Particle properties of ZrO<sub>2</sub>**

Parameter	Value
Solid density (kg/m <sup>3</sup> )	$5.89 \times 10^3$
Liquid density (kg/m <sup>3</sup> )	$5.89 \times 10^3$
Solid thermal conductivity (W/m/K)	2.0
Liquid thermal conductivity (W/m/K)	3.0
Solid specific heat (J/kg/K)	580
Liquid specific heat (J/kg/K)	713
Melting temperature (K)	2950
Boiling temperature (K)	5000
Latent heat of melting (J/kg)	$8 \times 10^5$
Latent heat of vaporization (J/kg)	$6 \times 10^6$

**Table 3 Solvent properties of ethanol**

Parameter	Value
Density (kg/m <sup>3</sup> )	$0.8 \times 10^3$
Specific heat (J/kg/K)	2400
Latent heat of vaporization (J/kg)	$9.25 \times 10^5$
Boiling temperature (K)	351

input to the plasma jet.  $T_w$  is the nozzle wall temperature, which has an initial value of 300 K. The velocity at the wall boundary is 0. The downstream flow of the jet is open.

The plasma flow field was solved using a cylindrical coordinate system. The radial distance was 6 cm with 57 grid points, and the axial distance was 8 cm with 66 grid points. The droplets and particles were tracked in the plasma flow field. For the nanoparticle, the temperature distribution and location of the melting interface were calculated using 50 grid points in spherical coordinates. The droplets had an initial temperature of 300 K, and velocity of 50 m/s. The initial diameter of the suspension droplets depends on the atomization method, atomizer conditions, and properties of the liquid. For a pneumatic atomizer, the droplet diameter generally ranges between 5 and 100  $\mu\text{m}$  (Ref 22). A mean droplet diameter of 50  $\mu\text{m}$  was assumed in this study.

## 4. Validation of Model Predictions

To study the complex particle behavior in plasma spray, the in-house numerical code LAVA-P-3D was developed. To validate this code, the calculated centerline gas temperature profile was compared with published numerical and experimental results. The experimental data were obtained by Brossa and Pfender, using a Sulzer Metco 3MB plasma spray gun (Ref 29). In addition to these experiments, numerical predictions by Jabbari et al. with FLUENT CFD software have also been included for comparison (Ref 17). Both the FLUENT simulation and this study used the  $k-\epsilon$  turbulence model with the same operating parameters of the plasma spray gun as used in the experiments of Brossa et al. As seen in Fig. 4, the projected gas temperature profile shows reasonable agreement with the experimental data and the FLUENT predictions. In the plasma core region, the LAVA-P-3D

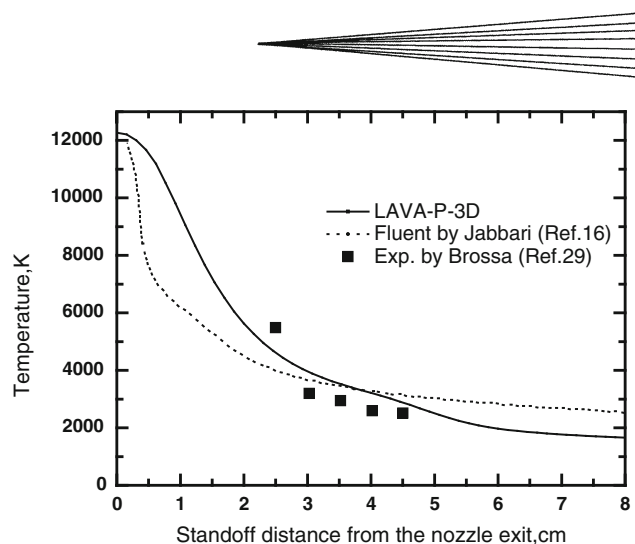


**Fig. 4** Comparison between the centerline gas temperature profile and published numerical results obtained using FLUENT software (Ref 17) and experimental data (Ref 29)

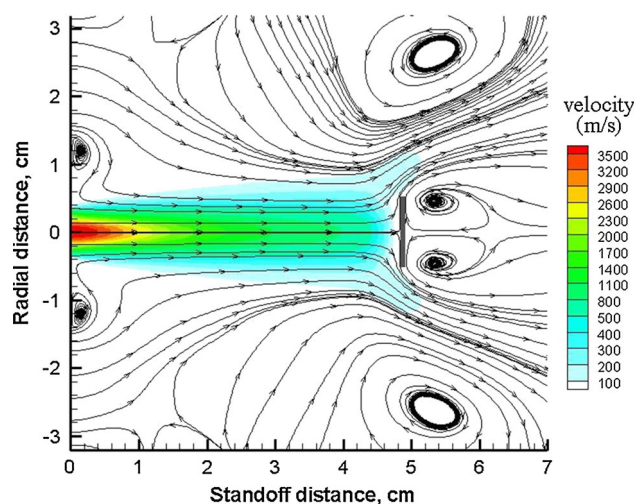


**Fig. 5** Gas velocity and streamlines in suspension plasma spray

code seems to give more realistic results than the FLUENT code. The hot core region with temperature higher than 5000 K extends from the nozzle exit to a position 2.3 cm downstream, which is close to the experimental value (2.8 cm), while the FLUENT result shows a shorter plasma core region (1.5 cm).

## 5. Discussion

### 5.1 Results for Plasma Jet Temperature and Velocity

The gas velocity and temperature are shown in Fig. 5 and 6. The hottest plasma zone extends from the torch exit to 1 cm, with temperature and velocity higher than 10,000 K and 3000 m/s, respectively. Outside the core region, the gas is decelerated and cooled steadily along the axial direction, and then passes around the substrate. The

substrate is illustrated as the gray plate at standoff distance of 5 cm, in Fig. 5 and 6. The substrate causes the fluid flow to form vortexes behind it, as well as on the two shoulders. The vortex flow decelerates the gas velocity rapidly near the substrate, and therefore may also slow down the particle. The temperature of the substrate facing the plasma torch becomes higher due to the heating effect of stagnant gas; meanwhile, on the backside of the substrate, the temperature decreases, due to the cooling effects of backside vortexes.

## 5.2 Effects of Particle Size

Depending on the nanoparticle size, the drag force, Saffman lift force, and Brownian force play different roles in the flight history. Figure 7–9 show the force magnitude for nanoparticles with diameters of 1, 10, and 100 nm, respectively. At the beginning of flight, the particles are embedded in the microdroplets, so the drag force is

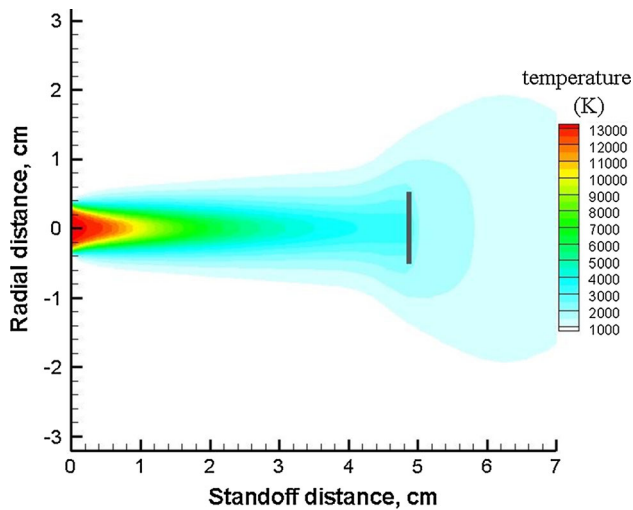


**Fig. 6** Gas temperature contours in suspension plasma spray

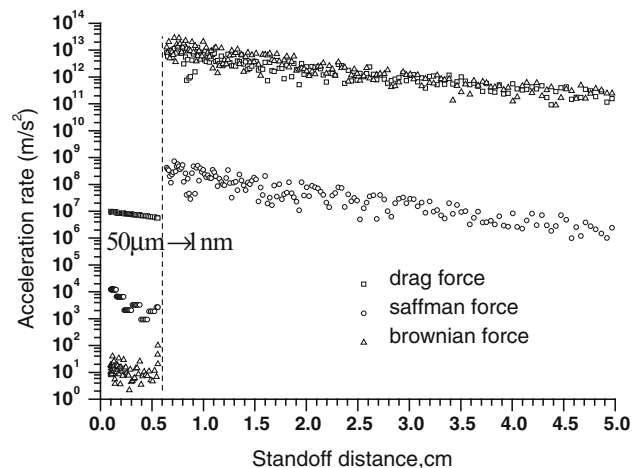


**Fig. 7** Force magnitudes on nanoparticle with diameter of 1 nm

dominant, the Saffman force is secondary, and the Brownian force is the smallest. When the nanoparticles are discharged into the plasma gas, at an axial distance of about 0.6 cm, all three forces increase, but the Brownian force increases most significantly compared with the drag force. The Saffman lift force is now the smallest among these three forces. The smaller the particle size, the larger the Brownian force.

The effects of particle size on velocity are depicted in Fig. 10. Before about 0.6 cm, all suspension droplets have similar velocity. After that, the nanoparticles are discharged into the plasma jet. Nanoparticles of different sizes have different speed histories. Particles with diameter less than 100 nm have larger acceleration, as a result of their small inertia. This means that, as expected, the nanoparticles can reach higher velocity when flying through the plasma core. When the nanoparticles reach a local gas velocity of about 2500 m/s, deceleration occurs. Compared with microparticles with diameter of 1000 nm (1  $\mu\text{m}$ ), nanoparticles have highly fluctuating velocity, due

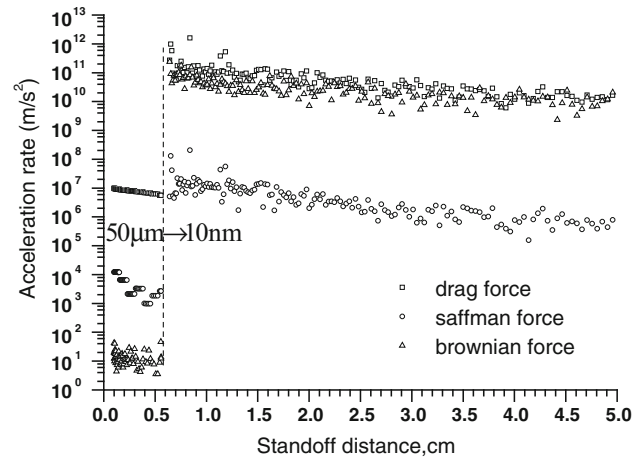


**Fig. 8** Force magnitudes on nanoparticle with diameter of 10 nm

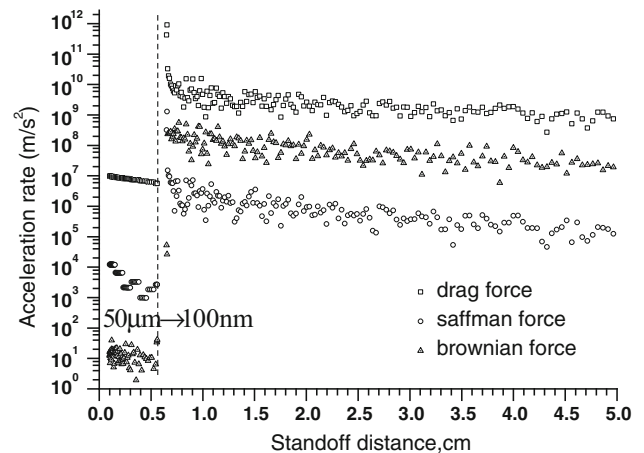


**Fig. 9** Force magnitudes on nanoparticle with diameter of 100 nm

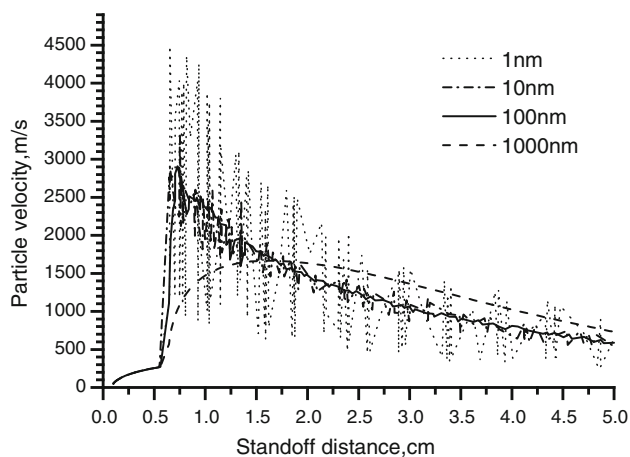


**Fig. 10** Effects of particle size on velocity

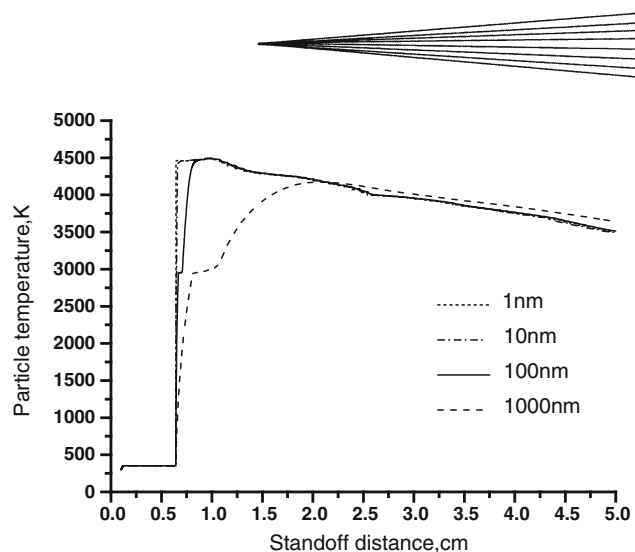


**Fig. 12** Effects of particle size on their temperature

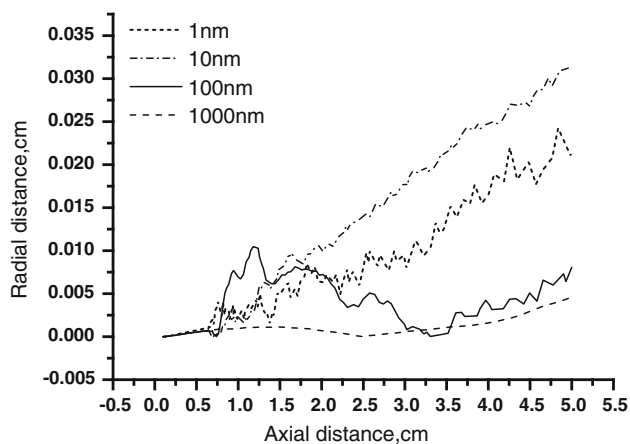


**Fig. 11** Effects of particle size on trajectory

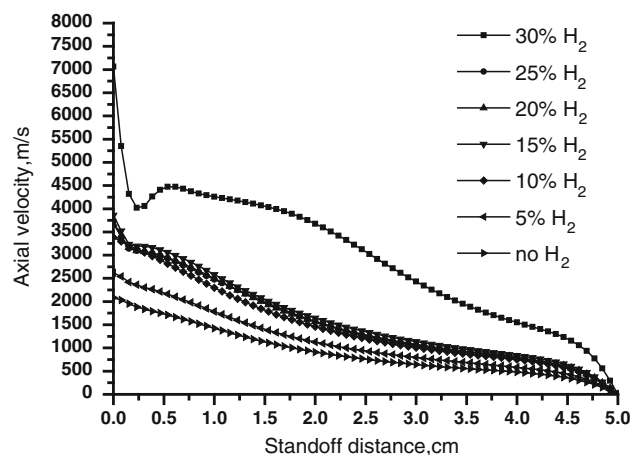


**Fig. 13** Effects of gas composition on the axial velocity at the centerline

to the effect of the large Brownian force. The smaller the particle, the larger the fluctuation amplitude. When arriving at the substrate, the microparticles might have a larger velocity than the nanoparticles. The reason is that the nanoparticles decelerate faster compared with the microparticles downstream in the plasma jet.

The trajectories of nanoparticles of different sizes are presented in Fig. 11. Results show that the nanoparticles with diameter less than 100 nm have chaotic trajectories due to the large Brownian force. A high degree of chaotic behavior in the nanoparticle trajectories might result in a wider spatial distribution of SPS, compared with conventional plasma spray using micrometer-size powder.

As shown in Fig. 12, the particle temperature undergoes three stages in the suspension spray process. Firstly, the microdroplet absorbs heat to evaporate the solvent. At this stage the droplet temperature is about 350 K. After the solvent has vaporized, the microagglomerate of nanoparticles will be discharged and their temperature increases immediately up to 4500 K. The temperature of the microparticles increases more slowly than that of the nanoparticles. Eventually, the particles will be cooled

down and some particles may resolidify. The microsized particles have a higher temperature than the nanoparticles due to their larger heat capacity and lower cooling rate.

### 5.3 Effects of Operating Conditions

The gas composition and electrical power input into the plasma gas are two key parameters in plasma spray processing. Figure 13 and 14 show the effect of gas composition on gas velocity and temperature at the torch centerline for power input of 50 kW. The total plasma gas flow rate was set at 240 slm, and the volume ratio of hydrogen in the plasma gas was varied from 0 to 30%. Results show that increasing the hydrogen ratio leads to more nanoparticles being discharged, because the enthalpy and thermal conductivity of hydrogen are larger than for argon. When the plasma flow has more hydrogen, the temperature of the jet is higher, so the solvent can be more easily vaporized and the nanoparticles more easily discharged. The higher the hydrogen ratio, the higher the gas velocity and temperature. The reason for the higher

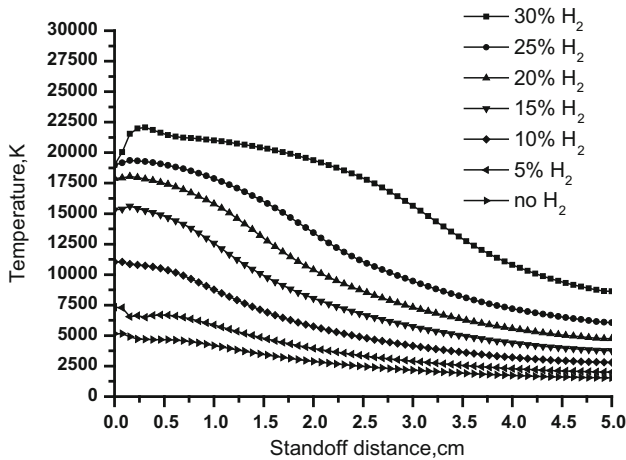


**Fig. 14** Effects of gas composition on the temperature at the centerline

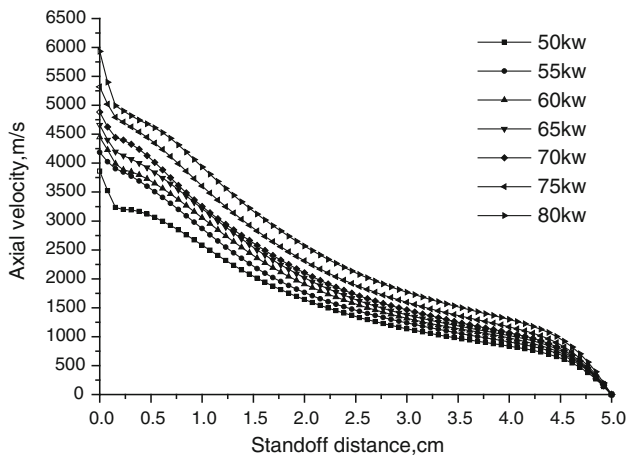


**Fig. 15** Effects of power input on the axial velocity at the centerline

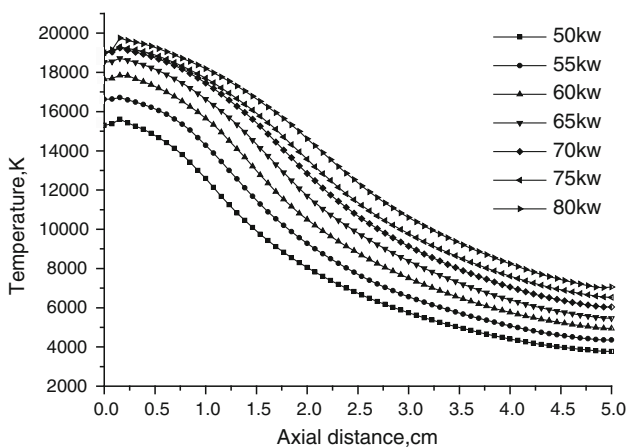


**Fig. 16** Effects of power input on the temperature at the centerline

gas velocity is that, as the temperature increases, the gas density decreases, so the velocity of the gas increases.

Power input is also a key parameter. Figure 15 and 16 show, for the same gas composition (15 vol.% hydrogen with 85 vol.% argon), simulation results for different power inputs from 50 to 80 kW. For higher power input, the gas velocity and temperature are higher, because high power input transfers more momentum and heat to the plasma gas, which increases the gas temperature and velocity.

## 6. Conclusions

In this study, a comprehensive model was developed to simulate the in-flight behavior of micro- and nanoparticles in a SPS process. The importance of the drag force, Saffman lift force, and Brownian force on particle movement and heating was investigated, as well as size effects and the influence of the plasma operating conditions. The results can be summarized as follows:

1. Brownian force plays a more prominent role for nanoparticles than microsized particles. For a microsized particle, the drag force is dominant. The Saffman lift force has more influence on microsized than on nanosized particles.
2. The nanoparticle acceleration and heating processes are quicker than for microsized particles, but at the substrate location, the microsized particles may have larger velocities, due to their greater inertia. The cooling process of microsized particles is slower than for nanoparticles.
3. Increasing the ratio of hydrogen or the power input causes the gas temperature and velocity to become larger. More nanoparticles could be discharged into the jets. Therefore, high hydrogen ratio and high power input are favorable for better nanoparticle discharge and better coating.

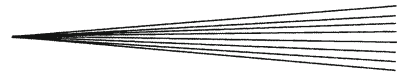
## Acknowledgments

The work was supported by the National Natural Science Foundation of China (nos. 11472245, 11072216, and 10602052) and the Fundamental Research Funds for the Central Universities (nos. 2012FZA4027).

## References

1. P. Fauchais, G. Montavon, R.S. Lima, and B.R. Marple, Engineering A New Class of Thermal Spray Nano-Based Microstructures from Agglomerated Nanostructured Particles, Suspensions and Solutions: An Invited Review, *J. Phys. D Appl. Phys.*, 2011, **44**(9), p 1-52
2. J. Karthikeyan, C.C. Berndt, J. Tikkanen, J.Y. Wang, A.H. King, and H. Herman, Preparation of Nanophase Materials by Thermal





- Spray Processing of Liquid Precursors, *Nanostruct. Mater.*, 1997, **9**, p 137-140
3. P. Fauchais and G. Montavon, Latest Developments in Suspension and Liquid Precursor Thermal Spraying, *J. Therm. Spray Technol.*, 2010, **19**, p 226-239
  4. U. Kogelschatz, Atmospheric-Pressure Plasma Technology, *Plasma Phys. Control. Fus.*, 2004, **46**, p B63-B75
  5. E.H. Jordan, M. Gell, Y.H. Sohn, D. Goberman, L. Shaw, S. Jiang, M. Wang, T.D. Xiao, Y. Wang, and P. Strutt, Fabrication and Evaluation of Plasma Sprayed Nanostructured Alumina-Titania Coatings with Superior Properties, *Mater. Sci. Eng. A*, 2001, **301**, p 80-89
  6. P. Fauchais, R. Etchart-Salas, C. Delbos, M. Tognovi, V. Rat, J.F. Coudert, and T. Chartier, Suspension and Solution Plasma Spraying of Finely Structured Coatings, *J. Phys. D Appl. Phys.*, 2007, **40**, p 2394-2406
  7. R.S. Lima, A. Kucuk, and C.C. Berndt, Integrity of Nanostructured Partially Stabilized Zirconia after Plasma Spray Processing, *Mater. Sci. Eng. A*, 2001, **313**, p 75-82
  8. F. Tarasi, M. Medraj, A. Dolatabadi, J. Oberste-Berghaus, and C. Moreau, Effective Parameters in Axial Injection Suspension Plasma Spray Process of Alumina-Zirconia Ceramics, *J. Therm. Spray Technol.*, 2008, **17**(5-6), p 685-691
  9. E. Meillot, S. Vincent, C. Caruyer, J.-P. Caltagirone, and D. Damiani, From DC Time-Dependent Thermal Plasma Generation to Suspension Plasma-Spraying Interactions, *J. Therm. Spray Technol.*, 2009, **18**, p 875-886
  10. D. Chen, E.H. Jordan, and M. Gell, The Solution Precursor Plasma Spray Coatings: Influence of Solvent Type, *Plasma Chem. Plasma Process.*, 2010, **30**, p 111-119
  11. P. Fauchais, R. Etchart-Salas, V. Rat, J.F. Coudert, N. Caron, and K. Wittmann-Teneze, Parameters Controlling Liquid Plasma Spraying: Solutions, Sols, or Suspensions, *J. Therm. Spray Technol.*, 2008, **17**(1), p 31-59
  12. A. Ozturk and B.M. Cetegen, Modeling of Axially and Transversely Injected Precursor Droplets into a Plasma Environment, *Int. J. Heat Mass Transf.*, 2005, **48**, p 4367-4383
  13. C. Marchand, C. Chazelas, G. Mariaux, and A. Vardelle, Liquid Precursor Plasma Spraying: Modeling the Interactions Between the Transient Plasma Jet and the Droplets, *J. Therm. Spray Technol.*, 2007, **16**(5-6), p 705-711
  14. A.M. Ahmed, R.H. Rangel, V.V. Sobolev, and J.M. Guilemany, In-Flight Oxidation of Composite Powder Particles During Thermal Spraying, *Int. J. Heat Mass Transf.*, 2001, **44**, p 4667-4677
  15. S. Basu, E.H. Jordan, and B.M. Cetegen, Fluid Mechanics and Heat Transfer of Liquid Precursor Droplets Injected into High-Temperature Plasmas, *J. Therm. Spray Technol.*, 2008, **17**, p 60-72
  16. Y. Shan and Y. Hu, Heat and Mass Transfer within an Evaporating Solution Droplet in a Plasma Jet, *J. Therm. Spray Technol.*, 2012, **21**(3-4), p 676-688
  17. F. Jabbari, M. Jadidi, R. Wuthrich, and A. Dolatabadi, A Numerical Study of Suspension Injection in Plasma-Spraying Process, *J. Therm. Spray Technol.*, 2014, **23**, p 3-13
  18. J.D. Ramshaw and C.H. Chang, Computational Fluid Dynamics Modeling of Multi-Component Thermal Plasmas, *Plasma Chem. Plasma Process.*, 1992, **12**, p 299-325
  19. Y.C. Lee, K.C. Hsu, and E. Pfender, Modeling of Particles Injected into a D.C. Plasma Jet, *5th International Symposium on Plasma Chemistry*, Edinburgh, Scotland, 1981
  20. X. Chen and E. Pfender, Behavior of Small Particles in a Thermal Plasma Flow, *Plasma Chem. Plasma Process.*, 1983, **3**(3), p 351-366
  21. X. Chen and E. Pfender, Effect of the Knudsen Number on Heat Transfer to a Particle Immersed into a Thermal Plasma, *Plasma Chem. Plasma Process.*, 1983, **3**, p 97-113
  22. H.B. Xiong and J.Z. Lin, Nanoparticles Modeling in Axially Injection Suspension Plasma Spray of Zirconia and Alumina Ceramics, *J. Therm. Spray Technol.*, 2009, **18**(5), p 887-895
  23. H.B. Xiong, L.L. Zheng, S. Sampath, R.L. Williamson, and J.R. Fricke, Three-Dimensional Simulation of Plasma Spray: Effects of Carrier Gas Flow and Particle Injection on Plasma Jet and Entrained Particle Behavior, *Int. J. Heat Mass Transf.*, 2004, **47**, p 5189-5200
  24. P.G. Saffman, The Lift on a Small Sphere in a Slow Shear Flow, *J. Fluid Mech.*, 1965, **22**(2), p 385-400
  25. K.C. Chung, Three-Dimensional Analysis of Airflow and Contaminant Particle Transport in a Partitioned Enclosure, *Build. Environ.*, 1999, **34**, p 7-17
  26. F. Peng and S.K. Aggarwal, A Review of Droplet Dynamics and Vaporization Modeling for Engineering Calculations, *J. Eng. Gas Turb. Power*, 1995, **117**, p 453-461
  27. Y.P. Wan, V. Prasad, G.-X. Wang, S. Sampath, and J.R. Fincke, Model and Powder Particle Heating, Melting, Resolidification, and Evaporation in Plasma Spraying Processes, *J. Heat Transf.*, 1999, **121**, p 691-699
  28. X. Chen and E. Pfender, Heat Transfer to a Single Particle Exposed to a Thermal Plasma, *Plasma Chem. Plasma Process.*, 1982, **2**(2), p 185-212
  29. M. Brossa and E. Pfender, Probe Measurements in Thermal Plasma Jets, *Plasma Chem. Plasma Process.*, 1988, **8**, p 75-90